PAPER

Check for updates

TiN/SiO$_2$ core–shell refractory plasmonic nanostructures unlock unprecedented 26.7% power conversion efficiency in Pb-free perovskite solar cells

Ahmed A. Mohsen,[a] Mohamed Zahran,[b] S. E. D. Habib[c] and Nageh K. Allam [ID] *[a]

TiN/SiO$_2$ core–shell refractory plasmonic nanoparticles have been utilized as highly efficient nanoantennas to enhance the performance of lead-free perovskite solar cells (PSCs). The SiO$_2$ shell, selected for its high refractive index and low extinction coefficient, enables precise light control while minimizing optical losses. A 3D finite element method (FEM)-based optoelectronic model was developed to analyze the optical and electrical characteristics of both unmodified and TiN/SiO$_2$-integrated PSCs. The results demonstrate a strong correlation between power conversion efficiency (PCE) and nanoparticle size. Incorporating 90 nm nanoparticles increases the PCE from 12.9% to 17.3%, while 115 nm nanoparticles achieve an impressive 26.7%, marking a 97.3% improvement. These findings highlight the pivotal role of tailored plasmonic nanostructures in maximizing light absorption and energy conversion. This study advances the understanding of plasmonic nanomaterials in photovoltaics and offers a viable strategy for enhancing the efficiency of lead-free PSCs. The integration of TiN/SiO$_2$ nanoparticles presents a promising pathway for developing high-performance, sustainable solar technologies.

Introduction

Over the past decade, research on lead (Pb)-based perovskite solar cells (PSCs) has surged due to their remarkable efficiency and cost-effectiveness.[1–6] The highest certified power conversion efficiency (PCE) for PSCs, as reported by the National Renewable Energy Laboratory (NREL), stands at 26.7%, making them competitive with silicon (Si) solar cells.[7–9] However, the toxicity of Pb remains a major obstacle to the commercialization of PSCs.[10–14] To address this, researchers have explored ionic substitution to mitigate toxicity.[15–18]

Tin (Sn) has emerged as a promising alternative, demonstrating a significant PCE improvement from 6% (ref. 18) to 12.2%,[19] positioning it as a viable Pb substitute.[20] Nevertheless, Sn-based PSCs still exhibit lower efficiency than their Pb-based counterparts. A key challenge limiting the PCE of thin-film solar cells (TFSCs) is insufficient light absorption due to inadequate active layer thickness. To overcome this, plasmonic light-trapping nanoparticles have been introduced to enhance absorption.[21–24] These nanoparticles amplify nanoscale light–matter interactions by coupling near-field electromagnetic waves (sunlight) to sub-wavelength regions, functioning as nanoantennas.[25–27] The effectiveness of plasmonic near-field enhancement depends on factors such as geometry, dielectric properties, surface roughness, and the surrounding medium.

Metallic nanoparticles, particularly gold (Au) and silver (Ag), have been employed to improve TFSC efficiency[28,29] by redirecting scattered light and coupling electromagnetic waves at air/metal interfaces through surface plasmon-guided modes.[30,31] However, noble metals are costly, exhibit narrow-band absorption and scattering, suffer from thermal instability, and are incompatible with CMOS technology. As an alternative, refractory plasmonic metal nitrides such as zirconium nitride (ZrN) and titanium nitride (TiN) have gained attention due to their tunable optoelectronic properties.[32–37]

Recent studies have demonstrated their potential, with ZrN/SiO$_2$ core/shell nanostructures enhancing the PCE of Pb-free perovskite solar cells from 12.9% to 20%.[37] Dielectric shells play a crucial role in preventing the plasmonic core from serving as a recombination center at the nanoparticle surface. Among the various dielectric materials, silicon dioxide (SiO$_2$) is one of the most extensively utilized shells for plasmonic nanoparticles due to its chemical stability and optical transparency.[38] The Hirsch research group demonstrated that modifying metallic nanoparticles into core–shell structures led to a redshift in their plasmon resonance frequency, shifting it into the near-infrared region—a phenomenon leveraged for photothermal therapy applications.[39] Furthermore, several experimental studies[40,41]

[a]Energy Materials Laboratory, Physics Department, School of Sciences and Engineering, The American University in Cairo, New Cairo 11835, Egypt. E-mail: nageh.allam@aucegypt.edu

[b]Nanotechnology Laboratory, Electronics Research Institute, Cairo, Egypt

[c]Electronics and Communications, Faculty of Engineering, Cairo University, Giza, Egypt

have shown that tuning the dielectric properties of the shell layer can effectively modulate plasmonic behavior. This approach has been particularly beneficial in enhancing the performance of plasmonic devices, such as inverted organic solar cells, by influencing photoelectric current and light–matter interactions.

In this study, we demonstrate the potential of TiN/SiO$_2$ core/shell nanoparticles to significantly enhance the efficiency of Pb-free perovskite solar cells (PSCs). By incorporating these nano-structures into the active layer, we project that the power conversion efficiency (PCE) could reach up to 26.7%, making Pb-free PSCs a viable alternative to their Pb-based counterparts.

Theory and optoelectronic modeling

TiN and ZrN are good alternative plasmonic nanostructures for applications in the visible light and near infrared spectral regions, they offer significant advantages over noble metals in terms of stability CMOS compatibility. In order to obtain the plasmonic core–shell nanoparticle scattering cross section, which is the ratio of the scattered power to the incident power at a large distance from the particle, we calculated the scattering cross section efficiency using eqn (1) and (2).

$$Q_{sca} = \frac{C_{sca}}{\pi a^2} \tag{1}$$

$$Q_{sca} = \frac{1}{2\pi a^2 I_a} \text{Re} \int_0^{2\pi} \int_0^{\pi} \left(E_{s\theta} H_{s\phi}^* - E_{s\phi} H_{s\theta}^* \right) r^2 \sin\theta \, d\theta \, d\phi \tag{2}$$

where a is the radius of the core–shell nanoparticle and I_a is the incident radiation intensity. Eqn (3) expresses the scattering efficiency in terms of Mie scattering.

$$Q_{sca} = \frac{2}{(ka)^2} \sum_{n=1}^{\infty} (2n+1)\left(|a_n|^2 + |b_n|^2\right) \tag{3}$$

The above expression is used to describe the scattering efficiency that is used for near field enhancement. Quinten

extended the discussion to aggregate the scattered radial field components.[42] The generalized form of the scattering efficiency is expressed *via* eqn (4):

$$Q'_{sca} = \frac{r^2}{\pi a^2} \int_0^{2\pi} \int_0^{\pi} E_s E_s^* \sin\theta \, d\theta \, d\phi \tag{4}$$

Upon applying those conditions, it was reported that TiN nanoparticles are good scatterers for applications in the near infrared.[34]

Two 3D electromagnetic wave (EMW) models have been constructed based on finite element method (FEM). The first model is used to calculate the interaction of sunlight electromagnetic radiation (AM 1.5G) with the proposed planar solar cell active layers based on Maxwell's equations of light propagation:

$$\frac{\partial H}{\partial t} = \frac{-1}{\mu} \nabla \times E \tag{5}$$

$$\varepsilon \frac{\partial E}{\partial t} = \nabla \times H - \sigma E \tag{6}$$

where H is the magnetic field, E is the electric field, μ is the permeability, ε is the electric permittivity, and σ is the electric conductivity.

This model is used to calculate the full field for the design introduced in Fig. 1a. For calculating the total generation rate and short circuit current (J_{sc}). The optical carrier generation rate (G_{opt}) per wavelength over the active layer volume is calculated using eqn (7).[43]

$$G_{opt}(\lambda) = \frac{\varepsilon'' |E|^2}{2\hbar} \tag{7}$$

The total generation rate (TGR) can be calculated by integrating the optical carrier generation over the simulated wavelength (λ) using eqn (8),[37] where the minimum and maximum
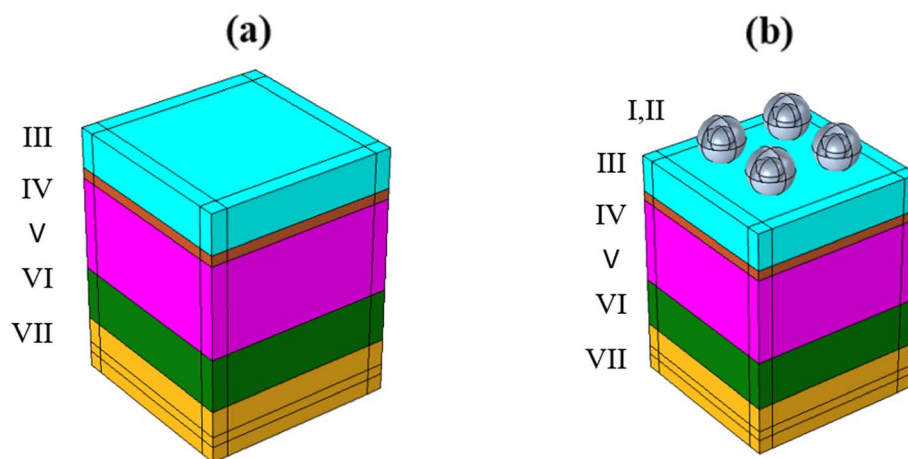

Fig. 1 (a) Planar perovskite solar cell structure consisting of (VII) gold (Au) as a back contact with a thickness of 100 nm, (VI) HTM (spiro-OMeTAD) with a thickness of 200 nm, (V) MASnI$_3$ active material with a thickness 350 nm, (IV) ETM (TiO$_2$) with thickness of 40 nm, and (III) ITO with thickness of 150 nm. (b) Planar perovskite with the core–shell nanoparticles consisting of (I) TiN nanoparticles as a plasmonic core and shielded by (II) SiO$_2$ nanoshells with thickness of 40 nm.

wavelengths that have been swept across the optical model are denoted by λ_1 and λ_2.

$$TGR = \int_{\lambda_1}^{\lambda_2} G_{opt}(\lambda)d\lambda \qquad (8)$$

The second model is based on coupling the first model as an input to simulate the nanostructured core/shell nanoparticles. TiN/SiO$_2$ nanoparticles are used as nanoantennas with different plasmonic core radii (50 nm, 75 nm) and a dielectric shell of 40 nm thickness decorated above the Sn-based PSc, as shown in Fig. 1b, and compare the localized surface plasmon enhanced PSC with the planar PSC design Fig. 1a. The normalized absorption is calculated using eqn (9).[44]

$$Normalized\ absorption = \frac{absorption\ of\ nanostructured\ film}{absorption\ of\ planar\ film} \qquad (9)$$

The external quantum efficiency (EQE) was obtained for the planar, TiN/SiO$_2$, nanostructured solar cells using eqn (10) assuming single-path absorption and unit internal quantum efficiency (IQE).[44]

$$EQE = IQE*\ absorption \qquad (10)$$

The optical refractive indices, extinction coefficients, and electrical parameters of Au, MASnI$_3$, TiO$_2$, spiro-OMeTAD, ITO, and TiN were extracted from previously published data.[45–53] G_{opt} was used as an input parameter in the electrical model. The drift-diffusion and 3D Poisson's equations were solved to determine the current–voltage characteristics. Series and shunt resistances were used as fitting parameters from previously measured data.[54] J_{sc} was calculated using eqn (11).[55]

$$J_{sc} = q \int_{\lambda_1}^{\lambda_2} \frac{AM\ 1.5G(\lambda) \times (1 - \exp(-\propto d))}{\frac{hc}{\lambda}}d\lambda \qquad (11)$$

where q is the elementary charge, d is the active layer thickness, and $\propto$ is the absorption coefficient calculated using eqn (12).

$$\propto = \frac{4\pi k(\lambda)}{\lambda} \qquad (12)$$

where $k(\lambda)$ is the extinction coefficient per wavelength. Since J_{sc} is directly proportional to the total carrier generation rate and have the same dimensions of the planar model, eqn (13) can be used to calculate any enhancement in J_{sc}.[56]

$$J_{sc}\ enhancement = \frac{total\ generation\ rate\ using\ nanostructures}{total\ generation\ rate\ of\ a\ planar\ cell} \qquad (13)$$

We integrated the AM 1.5G solar spectrum as an input power source into the Electromagnetic Waves Model in COMSOL Multiphysics. A wavelength range of 100–1350 nm was swept in 10 nm increments to encompass the UV, visible, and IR regions. This approach maximizes the enhancement effect in PSCs, as TiN exhibits increasing plasmonic activity in the IR band.[50,51] The PSC structure is enclosed by periodic boundary conditions (PBCs) along the x–y plane, while perfectly matched layers (PMLs) are applied in all directions to ensure accurate opto-electrical modeling.

Results and discussion

Core/shell-decorated nanoparticles

The optoelectrical model for a planar PSC is created first in order to compute the G_{opt} and J_{sc} for a planar PSC for better comparison before building the optoelectrical model of the TiN/SiO$_2$ core/shell-decorated PSCs. The TiN/SiO$_2$ core/shell structure has been employed to enhance the efficiency of PSCs, utilizing TiN cores with radii of 50 nm and 75 nm, each surrounded by a 40 nm SiO$_2$ shell. This core/shell configuration is designed to modulate the localized surface plasmon resonance (LSPR) of TiN, which is influenced by the surrounding dielectric medium. The proposed planar PSC design is shown in Fig. 1a, where the thicknesses of Au, spiro-OMeTAD, MASnI$_3$, TiO$_2$, and ITO layers are 100, 200, 40, 350, and 150 nm, respectively with 600 nm width. TiN/SiO$_2$ nanoparticles were implanted on-top of the PSC active layer as discussed in model 2 and shown in Fig. 1b. Fig. 2a–d shows the electric field profiles for planar perovskite solar cells after being illuminated by AM1.5G at different wavelengths of 300, 800, 1000, and 1200 nm, respectively.
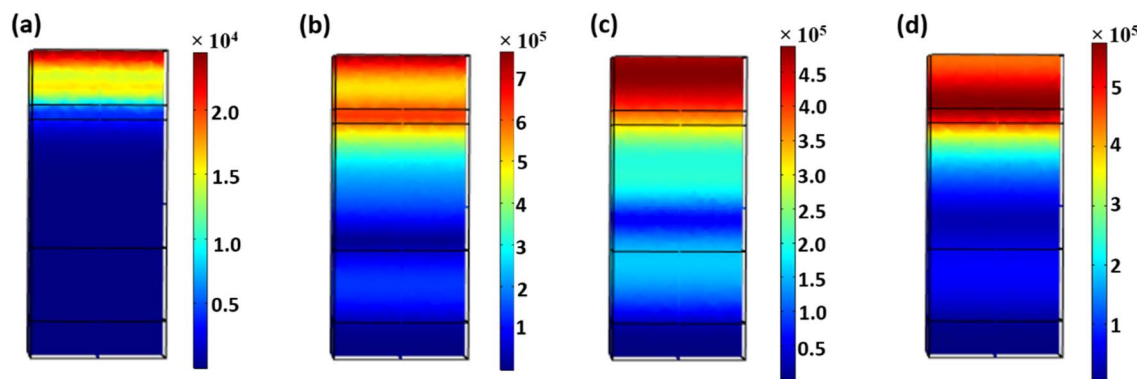

Fig. 2 Electric field profiles at different wavelengths: (a) 300 nm, (b) 800 nm, (c) 1000 nm, and (d) 1200 nm for planar PSCs.
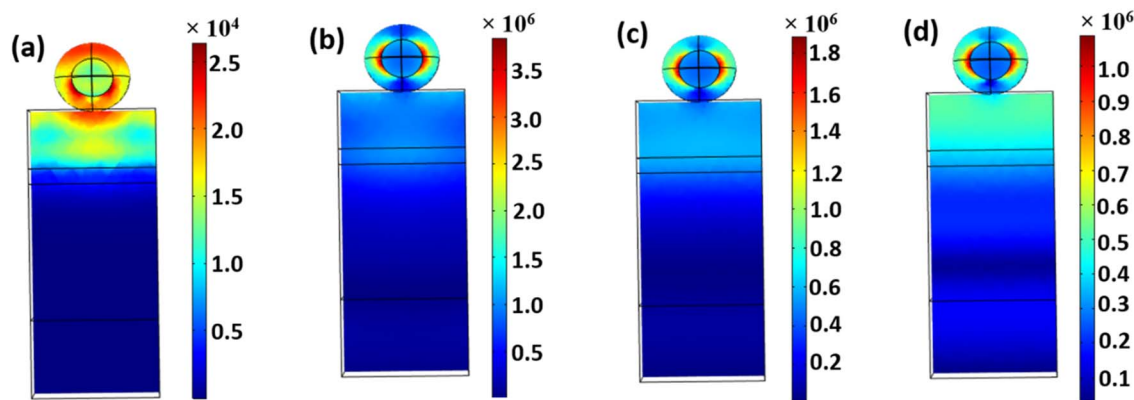
Fig. 3 Electric field profiles for TiN/SiO$_2$ core/shell decorated PSC with a core radius of 50 nm at different wavelengths: (a) 300 nm, (b) 800 nm, (c) 1000 nm, and (d) 1200 nm.

Fig. 3a–d illustrates the electric field profile after decorating the surface with TiN nanoparticles (50 nm radius) and a silica shell (40 nm thickness) at various frequencies spanning the visible, near-infrared (NIR), and infrared (IR) regions. At wavelengths of 800 nm and 1000 nm, a significant enhancement in the electric field coupling is observed. This enhancement is attributed to the localized surface plasmon resonance (LSPR) effect of TiN nanoparticles, which amplifies the local electric field in the NIR and IR regions, effectively coupling the incident electromagnetic wave into the active medium.

Fig. 4a–d presents the electric field profiles after embedding TiN/SiO$_2$ nanoparticles, where the TiN nanoparticles have a radius of 75 nm and the SiO$_2$ shell is 40 nm thick. While Fig. 4a shows the electric field profile at 300 nm, panels 4b and c demonstrate a significant enhancement in electric field coupling at a wavelength of 800 nm. This improvement is attributed to the high-quality factor of localized surface plasmon resonance (LSPR) within the 777–860 nm range, in agreement with the findings of Guler *et al.*, demonstrating TiN as an effective scatterer in the near-infrared (NIR) region.[57]

Using eqn (7), the corresponding optical generation rate (G_{opt}) is calculated for each simulated TiN/SiO$_2$ nanoparticle size and presented in Fig. 5a. TiN exhibits strong absorption within the 300–580 nm range, with a significant decline in its absorption coefficient beyond 780 nm. Notably, TiN/SiO$_2$ nanoparticles with a 90 nm radius exhibit a plasmonic peak near the infrared (IR) region, demonstrating high scattering capabilities. Meanwhile, PSCs decorated with 115 nm radius TiN/SiO$_2$ nanostructures show a plasmonic resonance peak at 880 nm, firmly within the IR spectrum.[51] As shown in Table 1, the transmission gain ratio (TGR), calculated using eqn (8), indicates a maximum enhancement of 97.3% for PSCs integrated with 115 nm TiN/SiO$_2$ nanoparticles compared to their planar counterparts.

Fig. 5b illustrates the normalized absorption, derived using eqn (9), for the simulated PSCs. TiN/SiO$_2$ nanoparticles act as nanocouplers, enhancing light absorption through their surface plasmon resonance (SPR) modes, which are effectively coupled to the PSC active layer. This enhancement is particularly significant in the IR range (>770 nm), where plasmonic nanoparticles function as waveguides, directing sunlight through localized SPR effects. This process generates surface plasmon polaritons (SPPs) at the air/TiN/SiO$_2$ nanoparticle interface, facilitating sub-wavelength light confinement within the active layer and improving overall solar absorption efficiency. Note the significant improvement in both the optical generation rate
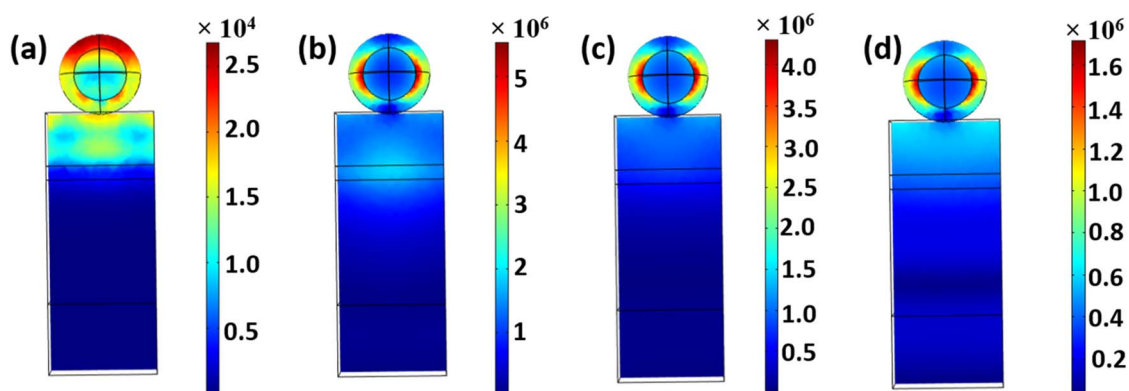

Fig. 4 Electric field profiles for TiN/SiO$_2$ core/shell decorated PSC with a core radius of 75 nm at different wavelengths: (a) 300 nm, (b) 800 nm, (c) 1000 nm, and (d) 1200 nm.
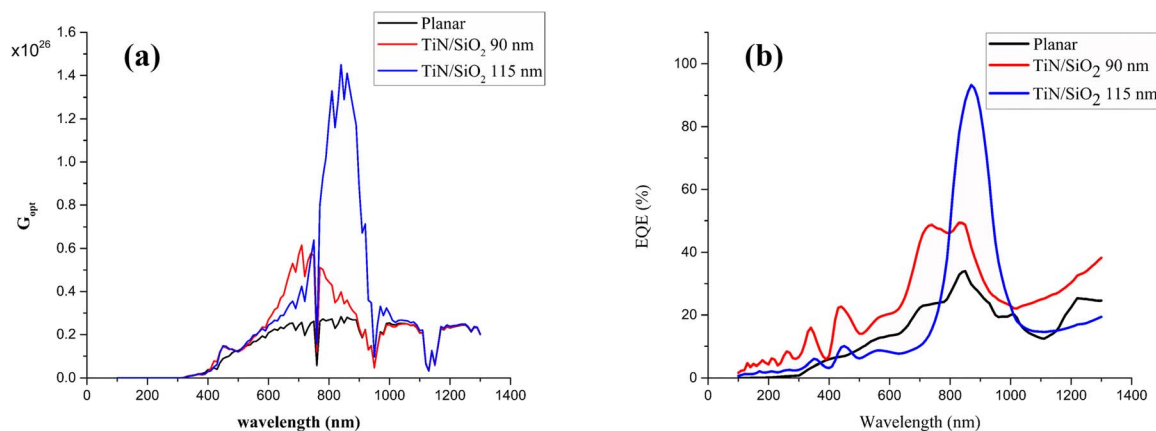
© 2025 The Author(s). Published by the Royal Society of Chemistry

Paper

Nanoscale Advances

Fig. 5 (a) Optical carrier generation rate (G_{opt}) and (b) normalized light absorption profiles for planar and TiN/SiO$_2$-decorated PSCs.

Table 1 The optical and electrical parameters of the TiN/SiO$_2$-decorated in comparison with previously published work ZrN/SiO$_2$ nanostructure PSCs

Structure	TGR (m^{-3} s^{-1})	TGR enhancement	J_{sc} (mA cm^{-2})	V_{oc} (mV)	FF (%)	PCE (%)
Planar	7.184×10^{27}	—	27	680.5	70.2	12.9
TiN/SiO$_2$ (90 nm)	9.441×10^{27}	31.42%	35.4	687.4	73.2	17.3
ZrN/SiO$_2$ (90 nm)[37]	9.1853×10^{27}	31%	34.5	687.4	71.2	16.9
TiN/SiO$_2$ (115 nm)	1.418×10^{28}	97.3%	53.2	691.4	95.8	26.7
ZrN/SiO$_2$ (115 nm)[37]	1.0721×10^{28}	55%	40.3	691.4	71.8	20

(G_{opt}) and optical absorption within the active layers of PSCs upon incorporating TiN/SiO$_2$ nanoparticles. Specifically, the substantial boost in optical generation at 710 nm for TiN/SiO$_2$ nanoparticles with a 90 nm radius, increasing from 2.56×10^{25} m^{-4} s^{-1} (planar) to 6.15×10^{25} m^{-4} s^{-1}. Additionally, for TiN/SiO$_2$ nanoparticles with a 115 nm radius, the optical generation
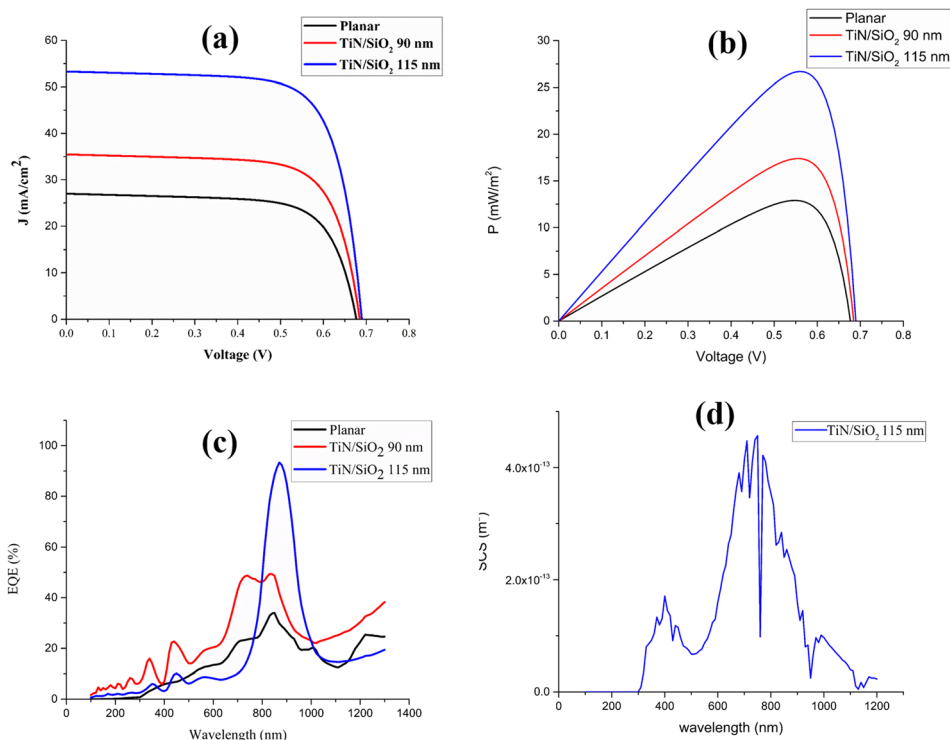

Fig. 6 (a) J–V, (b) P–V, (c) EQE, and (d) SCS characteristics of proposed TiN/SiO$_2$-decorated PSCs.

exhibits a remarkable enhancement at 860 nm, rising from 2.8×10^{25} m^{-4} s^{-1} to 1.41×10^{26} m^{-4} s^{-1}.

The J–V and P–V characteristics of TiN/SiO$_2$ core–shell nanostructured perovskite solar cells (PSCs) are shown in Fig. 6a and b and summarized in Table 1. Table 1 also recorded the TGR, FF, J_{sc} and PCE as compared to those previously reported in the literature.[37] The series and shunt resistances were optimized while considering recombination mechanisms in PSCs, as previously reported in the literature.[54] The optimal values were determined to be 50 Ω for series resistance and 400 Ω for shunt resistance. Incorporating TiN/SiO$_2$ nanoparticles significantly enhances the short-circuit current density (J_{sc}) compared to planar PSCs, as it is directly linked to optical generation enhancement. Table 1 reveals that embedding TiN/SiO$_2$ nanoparticles with a 90 nm radius increases the total generation rate (TGR) from 7.184×10^{27} m^{-3} s^{-1} to 9.441×10^{27} m^{-3} s^{-1}, leading to an increase in J_{sc} from 27 mA cm^{-2} to 35.4 mA cm^{-2}. Furthermore, using TiN/SiO$_2$ nanoparticles with a 115 nm radius results in a remarkable TGR enhancement from 7.184×10^{27} m^{-3} s^{-1} to 1.418×10^{28} m^{-3} s^{-1}, boosting J_{sc} from 27 mA cm^{-2} to 53.2 mA cm^{-2}.

Notably, PSCs decorated with 115 nm TiN/SiO$_2$ nanoparticles exhibit the highest power conversion efficiency (PCE), increasing from 12.9% (for planar PSCs) to 26.7%, representing an impressive 97.3% efficiency enhancement. Fig. 6c illustrates the external quantum efficiency (EQE) enhancement for the TiN/SiO$_2$-decorated PSCs. The PSC integrated with 115 nm TiN/SiO$_2$ nanoparticles achieves an EQE of 91%, aligned with the calculated scattering cross section (SCS) profile shown in Fig. 6d. This enhancement aligns with the localized surface plasmon resonance of TiN/SiO$_2$ nanoparticles at 880 nm, consistent with the findings by Shalaev et al.[34]

The remarkable 97.3% improvement in power conversion efficiency (PCE) of the TiN/SiO$_2$-decorated perovskite solar cells (PSCs) arises from a combination of optical, electronic, and thermal enhancement mechanisms. The TiN core exhibits strong localized surface plasmon resonance (LSPR), which concentrates the electromagnetic field and enhances photon absorption in the perovskite layer. The SiO$_2$ shell amplifies light scattering, increasing the optical path length without compromising charge transport. Plasmon-induced hot carrier generation contributes to more efficient charge separation and reduced recombination, while the dielectric shell prevents direct contact between metal and perovskite, minimizing trap states. Additionally, localized photothermal heating from TiN facilitates strain relaxation and defect passivation in the perovskite crystal lattice, improving material stability and carrier lifetimes. These effects collectively result in enhanced light harvesting, optimized charge extraction, and suppressed nonradiative losses, driving a substantial improvement in photovoltaic performance.

Conclusions

This study demonstrates the significant potential of TiN/SiO$_2$ core–shell nanoparticles in enhancing the efficiency of lead-free perovskite solar cells (PSCs). By incorporating 115 nm TiN/SiO$_2$ nanoparticles, the power conversion efficiency (PCE) surged from 12.9% in planar PSCs to 26.7%, marking a 97.3% improvement. The results highlight the crucial role of nanoparticle size, with 90 nm nanoparticles achieving a PCE of 17.3%, while 115 nm nanoparticles delivered the highest efficiency. A 3D finite element method (FEM)-based optoelectronic model was developed to analyze the optical and electrical properties of modified and unmodified PSCs. The findings reveal a strong correlation between PCE and nanoparticle dimensions, emphasizing the importance of tailored plasmonic structures for optimal solar energy harvesting. This research advances the understanding of plasmonic nanostructures in photovoltaics and offers a viable pathway for improving solar cell performance. The integration of TiN/SiO$_2$ nanoparticles presents a promising approach to developing high-efficiency, lead-free PSCs, contributing to the advancement of sustainable and next-generation solar technologies.

Data availability

The data supporting this article are included in the manuscript.

Conflicts of interest

The authors declare that they have no conflict of interest.

References

1 A. Kojima, K. Teshima, Y. Shirai and T. Miyasaka, Organometal Halide Perovskites as Visible-Light Sensitizers for Photovoltaic Cells, *J. Am. Chem. Soc.*, 2009, **131**, 6050–6051.

2 W. Sharmoukh, *et al.*, Recent progress in the development of hole-transport materials to boost the power conversion efficiency of perovskite solar cells, *Sustainable Mater. Technol.*, 2020, **26**, e00210.

3 M. M. Lee, J. Teuscher, T. Miyasaka, T. N. Murakami and H. J. Snaith, Efficient Hybrid Solar Cells Based on Meso-Superstructured Organometal Halide Perovskites, *Science*, 2012, **338**, 643–647.

4 A. E. Shalan, A. N. El-Shazly, M. M. Rashad and N. K. Allam, Tin–zinc-oxide nanocomposites (SZO) as promising electron transport layers for efficient and stable perovskite solar cells, *Nanoscale Adv.*, 2019, **1**, 2654–2662.

5 L. Yuan, *et al.*, Semi-transparent perovskite solar cells: unveiling the trade-off between transparency and efficiency, *J. Mater. Chem. A*, 2018, **6**, 19696–19702.

6 A. E. Shalan, *et al.*, Dopant-free hole-transporting polymers for efficient, stable, and hysteresis-less perovskite solar cells, *Sustainable Mater. Technol.*, 2020, **26**, e00226.

7 D. Yang, R. Yang, S. Priya and S. F Liu, Recent Advances in Flexible Perovskite Solar Cells: Fabrication and Applications, *Angew. Chem., Int. Ed.*, 2019, **58**, 4466–4483.

8 A. Rajagopal, K. Yao and A. K. Jen, Toward Perovskite Solar Cell Commercialization: A Perspective and Research Roadmap Based on Interfacial Engineering, *Adv. Mater.*, 2018, **30**, 1800455.

9 C. Zhao, Z. Zhou, M. Almalki, M. A. Hope, J. Zhao, T. Gallet, A. Krishna, A. Mishra, F. T. Eickemeyer, J. Xu and Y. Yang, Stabilization of highly efficient perovskite solar cells with a tailored supramolecular interface, *Nat. Commun.*, 2024, **15**, 7139.

10 A. N. El-Shazly, M. Y. Rezk, K. M Gameel and N. K. Allam, Electrospun Lead-Free All-Inorganic Double Perovskite Nanofibers for Photovoltaic and Optoelectronic Applications, *ACS Appl. Nano Mater.*, 2019, **2**, 7085–7094.

11 Y. Zong, *et al.*, Continuous Grain-Boundary Functionalization for High-Efficiency Perovskite Solar Cells with Exceptional Stability, *Chem*, 2018, **4**, 1404–1415.

12 M. G. Ju, *et al.*, Toward Eco-friendly and Stable Perovskite Materials for Photovoltaics, *Joule*, 2018, **2**, 1231–1241.

13 M. A. Green, A. Ho-Baillie and H. J. Snaith, The emergence of perovskite solar cells, *Nat. Photonics*, 2014, **8**(7), 506.

14 G. Li, Y. T. Liu, F. Yang, M. Li, Z. Zhang, J. Pascual, Z. K. Wang, S. Z. Wei, X. Y. Zhao, H. R. Liu and J. B. Zhao, Biotoxicity of halide perovskites in mice, *Adv. Mater.*, 2024, **36**(2), 2306860.

15 T. Krishnamoorthy, *et al.*, Lead-free germanium iodide perovskite materials for photovoltaic applications, *J. Mater. Chem. A*, 2015, **3**, 23829–23832.

16 C. Zuo and L. Ding, Lead-free Perovskite Materials $(NH_4)_3Sb_2I_xBr_{9-x}$, *Angew. Chem., Int. Ed.*, 2017, **56**, 6528–6532.

17 N. Wang, *et al.*, Solar Cells: Heterojunction-Depleted Lead-Free Perovskite Solar Cells with Coarse-Grained B-γ-CsSnI$_3$ Thin Films, *Adv. Energy Mater.*, 2016, **6**, 1601130.

18 F. Hao, C. C. Stoumpos, D. H. Cao, R. P. H. Chang and M. G. Kanatzidis, Lead-free solid-state organic–inorganic halide perovskite solar cells, *Nat. Photonics*, 2014, **8**, 489–494.

19 P. Pandey, S. Cho, J. Bahadur, S. Yoon, C. M. Oh, I. W. Hwang, H. Song, H. Choi, S. Hayase, J. S. Cho and D. W. Kang, 4-Phenylthiosemicarbazide Molecular Additive Engineering for Wide-Bandgap Sn Halide Perovskite Solar Cells with a Record Efficiency Over 12.2%, *Adv. Energy Mater.*, 2024, 2401188.

20 C. C. Stoumpos, C. D. Malliakas and M. G. Kanatzidis, Semiconducting Tin and Lead Iodide Perovskites with Organic Cations: Phase Transitions, High Mobilities, and Near-Infrared Photoluminescent Properties, *Inorg. Chem.*, 2013, **52**, 9019–9038.

21 U. W. Paetzold, W. Qiu, F. Finger, J. Poortmans and D. Cheyns, Nanophotonic front electrodes for perovskite solar cells, *Appl. Phys. Lett.*, 2015, **106**(17), 173101.

22 J. Lerme, *et al.*, Optical Properties of a Particle above a Dielectric Interface: Cross Sections, Benchmark Calculations, and Analysis of the Intrinsic Substrate Effects, *J. Phys. Chem. C*, 2013, **117**, 6383–6398.

23 S. Nishimura, *et al.*, Standing Wave Enhancement of Red Absorbance and Photocurrent in Dye-Sensitized Titanium Dioxide Photoelectrodes Coupled to Photonic Crystals, *J. Am. Chem. Soc.*, 2003, **125**, 6306–6310.

24 S. Ito, *et al.*, Fabrication of thin film dye sensitized solar cells with solar to electric power conversion efficiency over 10%, *Thin Solid Films*, 2008, **516**, 4613–4619.

25 P. J. Schuck, D. P. Fromm, A. Sundaramurthy, G. S. Kino and W. E. Moerner, Improving the Mismatch between Light and Nanoscale Objects with Gold Bowtie Nanoantennas, *Phys. Rev. Lett.*, 2005, **94**, 017402.

26 O. A. Abdelraouf, A. Shaker and N. K. Allam, Front dielectric and back plasmonic wire grating for efficient light trapping in perovskite solar cells, *Opt. Mater.*, 2018, **86**, 311–317.

27 A. Kinkhabwala, *et al.*, Large single-molecule fluorescence enhancements produced by a bowtie nanoantenna, *Nat. Photonics*, 2009, **3**, 654–657.

28 M. D. Kelzenberg, M. C. Putnam, D. B. Turner-Evans, N. S Lewis and H. A. Atwater, Predicted efficiency of Si wire array solar cells, *34th IEEE Photovoltaic Specialists Conference (PVSC) 001948-001953*, 2009.

29 W. Wang, S. Wu, K. Reinhardt, Y. Lu and S. Chen, Broadband Light Absorption Enhancement in Thin-Film Silicon Solar Cells, *Nano Lett.*, 2010, **10**, 2012–2018.

30 H. A. Atwater and A. Polman, Plasmonics for improved photovoltaic devices, *Nat. Mater.*, 2010, **9**, 205–213.

31 M. A. Schmidt and P. S. Russell, Long-range spiralling surface plasmon modes on metallic nanowires, *Opt. Express*, 2008, **16**, 13617.

32 A. E. Selmy, M. Soliman and N. K. Allam, Refractory plasmonics boost the performance of thin-film solar cells, *Emergent Mater.*, 2018, **1**, 185–191.

33 H. R. Stuart and D. G. Hall, Absorption enhancement in silicon-on-insulator waveguides using metal island films, *Appl. Phys. Lett.*, 1996, **69**, 2327–2329.

34 U. Guler, V. M. Shalaev and A. Boltasseva, Nanoparticle plasmonics: going practical with transition metal nitrides, *Mater. Today*, 2015, **18**, 227–237.

35 A. H. El-Saeed and N. K. Allam, Refractory plasmonics: orientation-dependent plasmonic coupling in TiN and ZrN nanocubes, *Phys. Chem. Chem. Phys.*, 2018, **20**, 1881–1888.

36 M. Kumar, N. Umezawa, S. Ishii and T. Nagao, Examining the Performance of Refractory Conductive Ceramics as Plasmonic Materials: A Theoretical Approach, *ACS Photonics*, 2015, **3**, 43–50.

37 A. A. Mohsen, M. Zahran, S. E. D. Habib and N. K. Allam, Refractory plasmonics enabling 20% efficient lead-free perovskite solar cells, *Sci. Rep.*, 2020, **10**(1), 6732.

38 S. Kalele, S. W. Gosavi, J. Urban and S. K. Kulkarni, Nanoshell particles: synthesis, properties and applications, *Curr. Sci.*, 2006, 1038–1052.

39 R. L. Hirsch, R. Jason Stafford, J. A. Bankson, S. R. Sershen, B. Rivera, R. E. Price, J. D. Hazle, N. J. Halas and J. L. West, Nanoshell-mediated near-infrared thermal therapy of tumors under magnetic resonance guidance, *Proc. Natl. Acad. Sci. U. S. A.*, 2003, **23**, 13549–13554.

40 L.-W. Jang, H. Park, S.-H. Lee, A. Y. Polyakov, R. Khan, J.-K. Yang and In-H. Lee, Device performance of inverted polymer solar cells with AgSiO$_2$ nanoparticles in active layer, *Opt. Express*, 2015, **23**(7), A211–A218.

41 K. N'Konou, M. Chalh, V. Monnier, N. P. Blanchard, Y. Chevolot, B. Lucas and P. Torchio, Impact of Ag@SiO$_2$ core-shell nanoparticles on the photoelectric current of plasmonic inverted organic solar cells, *Synth. Met.*, 2018, **239**, 22–28.

42 M. Quinten, Local fields close to the surface of nanoparticles and aggregates of nanoparticles, *Appl. Phys. B*, 2001, **73**(3), 245–255.

43 M. G. Deceglie, V. E. Ferry, A. P. Alivisatos and H. A. Atwater, Design of Nanostructured Solar Cells Using Coupled Optical and Electrical Modeling, *Nano Lett.*, 2012, **12**, 2894–2900.

44 O. A. Abdelraouf and N. K. Allam, Towards nanostructured perovskite solar cells with enhanced efficiency: coupled optical and electrical modeling, *Sol. Energy*, 2016, **137**, 364–370.

45 A. D. Rakić, A. B. Djurišić, J. M. Elazar and M. L. Majewski, Optical properties of metallic films for vertical-cavity optoelectronic devices, *Appl. Opt.*, 1998, **37**, 5271.

46 M. Roknuzzaman, *et al.*, Insight into lead-free organic-inorganic hybrid perovskites for photovoltaics and optoelectronics: a first principles study, *Org. Electron.*, 2018, **59**, 99–106.

47 X. Wang, G. Wu, B. Zhou and J. Shen, Optical Constants of Crystallized TiO$_2$ Coatings Prepared by Sol-Gel Process, *Materials*, 2013, **6**, 2819–2830.

48 M. Filipič, P. Loper, B. Niesen, S. De Wolf, J. Krč, C. Ballif and M. Topič, CH$_3$NH$_3$PbI$_3$ perovskite/silicon tandem solar cells: characterization based optical simulations, *Opt. Express*, 2015, **23**, A263–A278.

49 T. A. F. Konig, *et al.*, Electrically Tunable Plasmonic Behavior of Nanocube–Polymer Nanomaterials Induced by a Redox-Active Electrochromic Polymer, *ACS Nano*, 2014, **8**, 6182–6192.

50 V. Schnabel, R. Spolenak, M. Doebeli and H. Galinski, Structural Color Sensors with Thermal Memory: Measuring Functional Properties of Ti-Based Nitrides by Eye, *Adv. Opt. Mater.*, 2018, **6**, 1800656.

51 *RIT Nanolithograpy Research Labs*, **http://www.rit.edu/lithography**, accessed January 2025.

52 M. Lazemi, S. Asgharizadeh and S. Bellucci, A computational approach to interface engineering of lead-free CH$_3$NH$_3$SnI$_3$ highly efficient perovskite solar cells, *Phys. Chem. Chem. Phys.*, 2018, **20**, 25683–25692.

53 S. Bishnoi and S. K. Pandey, Device performance analysis for lead-free perovskite solar cell optimization, *IET Optoelectron.*, 2018, **12**, 185–190.

54 W. Ke, *et al.*, Efficient Lead-Free Solar Cells Based on Hollow MASnI$_3$ Perovskites, *J. Am. Chem. Soc.*, 2017, **139**, 14800–14806.

55 L. Debbichi, *et al.*, Perovskite Solar Cells: Mixed Valence Perovskite Cs$_2$Au$_2$I$_6$: A Potential Material for Thin-Film Pb-Free Photovoltaic Cells with Ultrahigh Efficiency, *Adv. Mater.*, 2018, **30**, 1870080.

56 O. A. Abdelraouf, A. Shaker and N. K. Allam, Novel design of plasmonic and dielectric antireflection coatings to enhance the efficiency of perovskite solar cells, *Sol. Energy*, 2018, **174**, 803–814.

57 U. Guler, G. Naik, A. Boltasseva, V. M. Shalaev and A. V. Kildishev, Performance analysis of nitride alternative plasmonic materials for localized surface plasmon applications, *Appl. Phys. B*, 2012, **107**, 285–291.